The crystallization mechanism of gel-derived SiO2-TiO2 amorphous nanobeads elucidated by high-temperature in-situ experiments

Alessio Zandonà, Emmanuel Véron, Gundula Helsch, Aurélien Canizarès, Joachim Deubener, Mathieu Allix, Cécile Genevois

The crystallization mechanism of gel-derived SiO_2-TiO_2 amorphous nanobeads elucidated by high-temperature in-situ experiments

Alessio Zandonà[a,b,*], Emmanuel Véron[a], Gundula Helsch[c], Aurélien Canizarès[a], Joachim Deubener[c], Mathieu Allix[a], Cécile Genevois[a,*]

[a] CNRS, CEMHTI UPR3079, Univ. Orléans, F-45071 Orléans, France

[b] Friedrich-Alexander-Universität Erlangen-Nürnberg, Department of Materials Science (Glass and Ceramics), 91058 Erlangen, Germany

[c] Clausthal University of Technology, Institute of Non-Metallic Materials, 38678 Clausthal-Zellerfeld, Germany

Abstract

SiO_2-TiO_2 amorphous nanobeads with a TiO_2 content up to 50 mol% were synthesized by sol-gel spray-drying. Their crystallization during heat treatments was then characterized by in-situ high-temperature techniques including X-ray diffraction, Raman spectroscopy and particularly high-resolution transmission electron microscopy. Intrinsic nanoscale chemical modulations could be identified already in the as-prepared nanobeads and were shown to play a major role for the non-isochemical precipitation of TiO_2 nanocrystals during heating experiments: the size and compositional contrast of such fluctuations progressively evolved and increased until the emergence of long-range ordering. The formation of TiO_2 polymorphs occurred according to Ostwald's rule of stages, with the metastable TiO_2(B) phase acting as precursor to stabilize anatase and rutile. The temporary appearance of TiO_2(B) nanocrystals at early annealing stages was interpreted as the first direct experimental observation of subcritical crystalline nuclei.

Keywords: high-temperature in-situ TEM experiments; crystal nucleation; subcritical nuclei; SiO_2-TiO_2 glasses; nanoscale compositional fluctuations

***Corresponding authors:** alessio.zandona@fau.de; cecile.genevois@cnrs-orleans.fr

1. Introduction

The term "crystallization" encompasses a wide range of reactions leading to the emergence of long-range periodicity in an initially amorphous or disordered substance, which can be also kinetically described by the interplay of crystal nucleation and growth processes. Be it from an oversaturated solution, vapour, glass or melt, crystal nucleation and growth are indeed ubiquitous processes in nature, with an extremely high economic relevance: controlling the final type, size and microstructure of crystalline products is crucial to design the properties of materials as disparate as food[1], drugs[2] and

technological (glass-)ceramics[3,4]. In-situ experimental investigation of crystallization processes from disordered precursors has therefore attracted a strong interest in the last decades, particularly with transmission electron microscopy (TEM) providing unrivalled possibilities to elucidate crystal nucleation and growth down to the nanoscale. Due to the undeniable challenges related to in-situ TEM experiments (especially during heating), previous studies have however mainly analysed structural rearrangements in metallic glasses (for instance[5–7]), while only few authors attempted to elucidate nucleation processes in an aqueous solution[8] or in semiconductor glasses such as fluorides[9] and oxides[10,11].

Consequently, we present in this work our most recent endeavours to push the envelope of direct in-situ characterization of phase separation and crystallization processes occurring at the nanoscale in an oxide glass (i.e. an undercooled melt) during thermal annealing. Our study features the use of a heating stage in both TEM and scanning (STEM) mode and the combination of nanoscale imaging, electron diffraction and electron energy loss spectroscopy (EELS). For such pioneering investigation, we selected gel-derived amorphous nanobeads of the compositional system SiO_2-TiO_2, since: (i) these simple binary glasses and glass-ceramics possess long-standing technological interest due to their low or zero thermal expansion[12] and applications in catalysis[13,14]; (ii) the absence of highly mobile species under the electron beam (such as alkali ions) and the high structural interconnectivity of these glasses[15,16] should guarantee a comparatively low susceptibility to beam damage; (iii) Si and Ti exhibit a good Z contrast for STEM imaging; (iv) nanobeads are easily handled for TEM experiments and all other supporting analytical techniques, as they can be observed in their as-prepared state, without specific preparation steps (e.g. polishing or grinding, thin foil preparation) which may induce modifications in the original material; (v) the formation of TiO_2-bearing crystals in undercooled silicate melts is interesting due to its common exploitation to induce volume nucleation in glass-ceramics[4]. Our results provide unprecedented insight into the phenomena leading to crystallization in SiO_2-TiO_2 glasses, thereby stressing the recently proposed importance of compositional fluctuations and medium-range order for crystal nucleation and growth[17].

2. Experimental

2.1 Synthesis of the amorphous nanobeads

The full synthesis protocol of sol-gel spray-dried SiO_2-TiO_2 nanobeads has been detailed elsewhere[14]. Isopropanol-based solutions containing as precursors tetraethoxysilane (TEOS, 99.0% (GC), Fluka) and Ti-butoxide (97.0%, Sigma-Aldrich) were atomized and channelled through a tube furnace set at 200 °C, recovering the dried nanobeads in a filter at the other end. Using this method, samples with 10, 17 and 50 mol% TiO_2 content were produced, respectively named T10, T17 and T50 in the following. Our analysis was centered on T17 and T50 due to their higher TiO_2 content and stronger tendency to crystallize, which favoured their examination by high-temperature in-situ analytics; the sample T10 was only used to evaluate the homogeneity of sol-gel spray-dried materials at lower TiO_2

content. The as-prepared materials still contained rests of their organic precursors, which were decomposed during an additional heat treatment at 450 °C for 12 h, based on the results of a previous work[14]. Silanol groups trapped in the glass structure were instead far more persistent, so that full dehydration was only achievable at temperatures and timescales comparable to or higher than those necessary for crystal nucleation[16].

2.2 Variable-temperature X-ray diffraction

Variable-temperature X-ray diffraction (VT-XRD) measurements were performed by loading the nanobeads into an Al_2O_3 crucible, placing a platinum foil on the bottom to avoid undesired reactions with the container. The crystallization sequence was then characterized using a D8 Advance Bruker laboratory diffractometer (Cu radiation, LynxEye XE line detector) equipped with an Anton Paar HTK1200N heating chamber. Measurements were performed during heating in the range 600-1200 °C for T17 (temperatures were chosen on the base of previous results[14,16]) and 300-1200 °C for T50 (due to the expected higher reactivity), acquiring a diffraction pattern every 50 °C; each isothermal measurement step lasted ~30 min, with 30 K min^{-1} ramps in between. Quantification of phase fractions and average crystallite sizes was performed using the TOPAS Academic V.6 Software[18], estimating line profiles by the fundamental parameters approach[19] (some representative fits are reported as Fig. S1 and S2 in the Supporting Information file).

2.3 Variable-temperature Raman spectroscopy

The as-prepared nanobeads still yielded strong photoluminescence upon laser irradiation, which was attributed to a residual content of organic precursors (in agreement with previous results[14]); for this reason, sample T17 was additionally treated at 600 °C for 12 h, to decompose these residues and therefore be able to acquire Raman spectra from the beginning of the variable-temperature (VT-)Raman experiments. For sample T50, such a treatment led to undesired crystallization; nanobeads treated at 450 °C for 12 hours (as for VT-XRD and in-situ TEM measurements) were therefore used for the Raman measurements. Our Renishaw InVia Qontor spectrometer mounted a blue laser (488 nm) operated at 40 mW (nominal power, reduced to 5% for sample T50 to avoid detector saturation) and was equipped with a Linkam TS 1500 heating stage. For the measurements, a small amount of nanobeads was deposited on a sapphire disk at the bottom of the heating chamber. The heating rate was set to 20 K min^{-1} and spectra were collected continuously in the range 100-2200 cm^{-1} (edge filter at ~150 cm^{-1}), also during the isothermal hold at the maximum temperatures (850 °C for T17 and 650 °C for T50), with: 15 s exposure, 4 acquisitions per spectrum. The free cooling rate achieved an average of 200 K min^{-1}; sample T17 was additionally reheated a second time to the maximum temperature (850 °C) after completion of the experiment, to evaluate the effect of temperature broadening on its Raman spectrum. The spectra are shown in their raw form, without the application of a Bose-Einstein temperature correction.

2.4 (Variable-temperature in-situ) transmission electron microscopy

Transmission Electron Microscopy (TEM) experiments were performed using a JEOL ARM200F (JEOL Ltd.) Cold FEG microscope operating at 80 kV, equipped with a double spherical aberration corrector, a Gatan Imaging Filter (GIF, Gatan Ltd.) and a One View camera. For conventional experiments, the nanobeads were dispersed in ethanol and one drop of the resulting suspension was deposited on a copper grid layered by a holey amorphous carbon film and dried in air. This preparation was used to evaluate the chemical homogeneity of as-prepared T10, T17 and T50 nanobeads (directly after the spray-drying synthesis) in scanning transmission electron microscopy mode by annular dark field imaging (STEM-ADF) and by spectrum-imaging electron energy loss spectroscopy (SI-EELS). SI-EELS data were acquired in DUAL-EELS mode to remove plural scattering effects and to realign the spectra based on the zero-loss peak a posteriori.

For experiments performed in situ at high temperature, the ethanol suspension containing nanoparticles pre-treated at 450 °C for 12 h was loaded onto a MEMS grid specifically adapted for a Protochips Fusion double-tilt heating holder. Before performing the heating experiments, we carefully evaluated the effects of the electron beam on the samples in order to minimize possible artefacts such as amorphization, crystallization or even evaporation frequently reported during in-situ characterization of both solids and liquids[20–22]. After some preliminary tests, we determined an approximate beam current threshold of 32 pA (measured from the fluorescent screen) below which it is possible to image SiO_2-TiO_2 glasses during heating for several tens of minutes in the temperature range of interest (RT – 600 °C on the temperature controller) with a generally good agreement with the crystallization sequence determined by VT-XRD and VT-Raman spectroscopy. The energetic contribution of the electron beam was still evident through the substantial reduction (by at least 200 or 300 °C) of the temperatures at which reactions took place. Heating to temperatures higher than 600 °C was instead avoided due to the occurrence of phenomena such as nanobead deformation, sample evaporation and reduction of Si and Ti to the metallic state, which manifested that beam damage and/or to the effect of vacuum started to prevail over thermally activated processes.

First, the crystallization of T50 was monitored in situ by high resolution transmission electron microscopy (HRTEM) imaging, during heating from room temperature to 600 °C at 300 K min^{-1}, with isothermal dwells of 5 min every 50 K (the time-temperature curve is provided on Fig. S3). During the experiment, micrographs were continuously recorded (image acquisition time: 1 s) with a resolution of 1K×1K over an area of ~50×50 nm^2, manually compensating for the sample drift and focus during heating. A similar experiment was performed on T17 and is mostly documented in the Supporting Information file; in this case, images (acquisition time: 1 s) were collected with a resolution of 4K×4K over an area of ~100×100 nm^2, lowering the magnification during the heating ramps to better adjust for the sample drift. Prior to the treatment, the so-collected data were manually resampled (10 representative micrographs for each isothermal dwell) and realigned to accommodate for sample drift in two steps, first manually and then automatically using the software DigitalMicrograph GMS.3 (Gatan).

The Protochips Fusion double-tilt heating holder was also used to characterize T50 by STEM-HAADF imaging and SI-EELS at various stages of heat treatment. To do so, the nanobeads (pre-treated at 450 °C for 12 h) were annealed in situ in the TEM, with a series of isothermal dwells of 5 min at gradually increasing temperatures, between 300 °C and 900 °C; in all cases, these dwells were respectively preceded and followed by quick heating and cooling ramps at 300 K min^{-1}. The observations were performed at room temperature after each cooling, making sure to always collect the data at locations that had never experienced direct electron irradiation at previous stages of the experiment.

3. Results and discussion

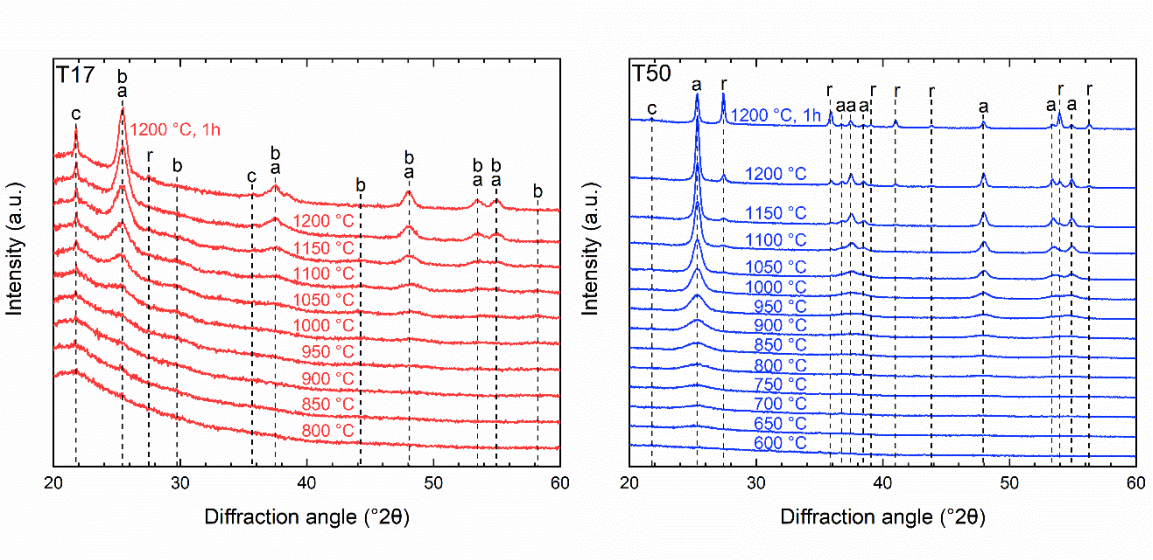

Figure 1. VT-XRD results for samples T17 and T50. Legend keys: *a* for anatase, *r* for rutile, *b* for TiO_2(B), *c* for cristobalite.

The amorphous nanoparticles T17 and T50 were first characterized by VT-XRD to gain a general idea of their crystallization sequence (Figs. 1 and 2). In T17, peaks assignable to cristobalite (minor), anatase and TiO_2(B) emerged simultaneously at 900-950 °C. The latter phase exhibited very broad and weak reflections, but its identification was unequivocal and supported by the results of full-pattern Rietveld refinements for phase quantification (Fig. S1). It was only distinguishable up to 1150 °C, while traces of rutile were first identifiable after reaching 1200 °C. The average crystallite size of TiO_2(B) was ~2 nm at its earliest appearance and never exceeded ~4 nm during the heat treatments (Fig. 2), i.e. it remained substantially smaller than that of anatase at the same temperatures (between 5 and 9 nm). In T50, instead, broad features related to anatase developed at 650 °C with an associated average crystallite size of ~3 nm; at 1050 °C, rutile appeared and gradually became the dominant phase, maintaining a very similar crystallite size to that of anatase all along the heat treatment and finally reaching ~40 nm at 1200 °C. The strong difference in final crystallite sizes achieved in the two samples is likely to originate from the much higher total TiO_2 content in T50 and from the presence in T17 of a

SiO_2-enriched, viscous residual melt up to high temperatures, acting as barrier for diffusion and particle coalescence.

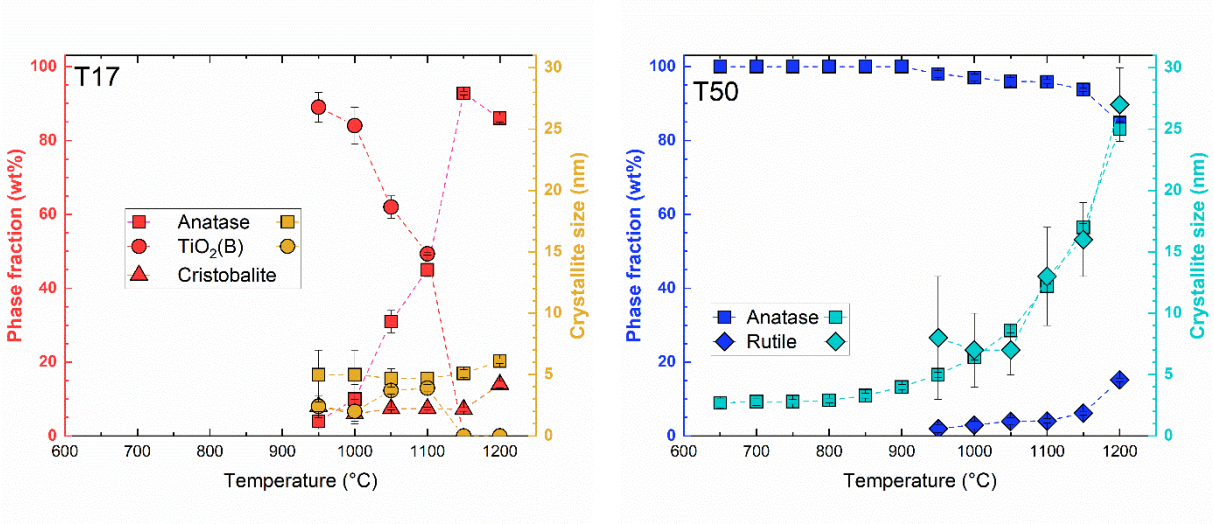

Figure 2. Phase fractions and average crystallite sizes (the latter not computed for cristobalite due to the low phase fraction) extracted from Rietveld refinements of the VT-XRD measurements performed on T17 and T50 nanobeads.

The formation of metastable TiO_2 polymorphs during crystal nucleation is a long-known phenomenon in glasses, typically involving anatase but recently also identified in the case of TiO_2(B) (see for instance[14,16,23]). It can be related to two main factors: (i) a stabilization effect due to small crystallite sizes and high surface-to-volume ratios, as demonstrated for anatase[24,25] and previously postulated for TiO_2(B) nanocrystals[14]; (ii) the energetic gain of gradually approaching the equilibrium configuration (rutile, the only thermodynamically stable polymorph) through several kinetically favoured intermediate steps, as theorized in Ostwald's rule of stages[26]. Indeed, TiO_2(B) exhibits low density and a very distorted 6-fold oxygen coordination around Ti^{4+} cations, representing an ideal "missing link" between the prevailing tetrahedral coordination in SiO_2-TiO_2 glasses[16] and the regular octahedral coordination of anatase and rutile.

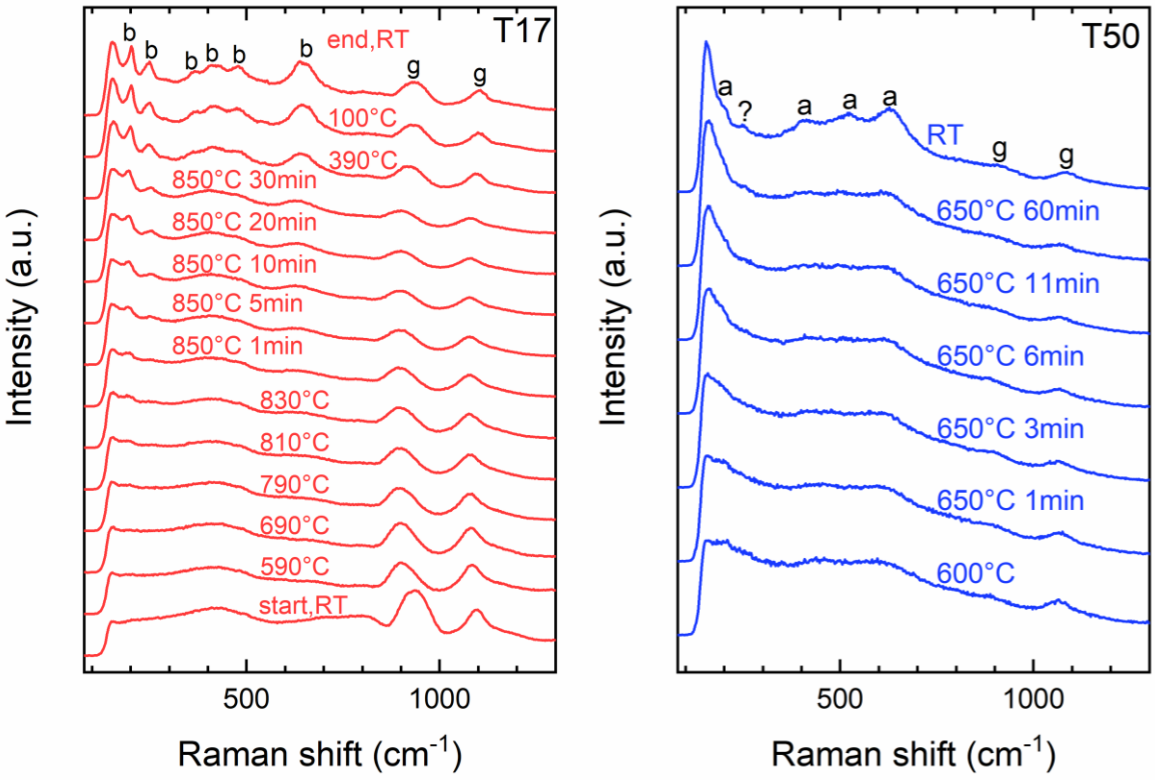

Figure 3. Spectra acquired from samples T17 and T50 during VT-Raman experiments. Labels highlight the most prominent Raman features of the formed phases: *a* for anatase, *b* for TiO_2(B), *g* for bands associated to Ti^{4+} incorporation in a SiO_2-TiO_2 glass, *?* for an unassigned peak.

We used VT-Raman spectroscopy to gain information on the early crystal nucleation stages of the T17 and T50 nanobeads. As demonstrated in previous works, Raman spectroscopy is a particularly effective tool to unambiguously discern different TiO_2 polymorphs precipitating in glasses, even for crystalline fractions of only a few vol%[14,16,23]. The Raman spectra of TiO_2(B) and anatase can be easily distinguished through several bands which are characteristic of monoclinic TiO_2(B) but absent in tetragonal anatase[27], e.g. at ~125 cm^{-1} (invisible here due to the edge filter) and at 250 cm^{-1}. Note that measurements at high temperature expectedly induced a non-negligible broadening and shift of Raman features that may complicate their interpretation, as exemplified during the reheating of T17 to 850 °C (Fig. 3). Nonetheless, our measurements clearly revealed that TiO_2(B) formed as first crystalline phase in T17, being retained down to room temperature; the simultaneous presence of anatase traces in the sample cannot be completely ruled out due to band overlap.

TiO_2(B) was instead virtually absent in T50, since only the peak labelled as "?" could tentatively be assigned to a small amount of this phase, while all other Raman features, initially extremely broad but eventually sharper, matched well with the spectrum of anatase. The direct appearance of this phase (in agreement with the VT-XRD data) is to be interpreted based on the composition of the starting

material, much richer in TiO_2 than T17: the structure around Ti^{4+} ions in T50 can be expected to mirror more closely that of TiO_2 crystals, not requiring an additional intermediate step (i.e. TiO_2(B) formation) to lower the energy barrier for nucleation. A residual amorphous silicate phase[16], evidently still containing a non-negligible amount of TiO_2 due to the intense Raman bands observable at 900 cm^{-1} and 1100 cm^{-1}, could still be detected in both samples after the measurements. This is in qualitative agreement with the results of VT-XRD, according to which the samples contained only a very small amount of anatase and/or TiO_2(B) at the temperatures then investigated by VT-Raman. Similarly, the broadness of the observed Raman features matches well with the XRD-derived nanosize of the formed crystals.

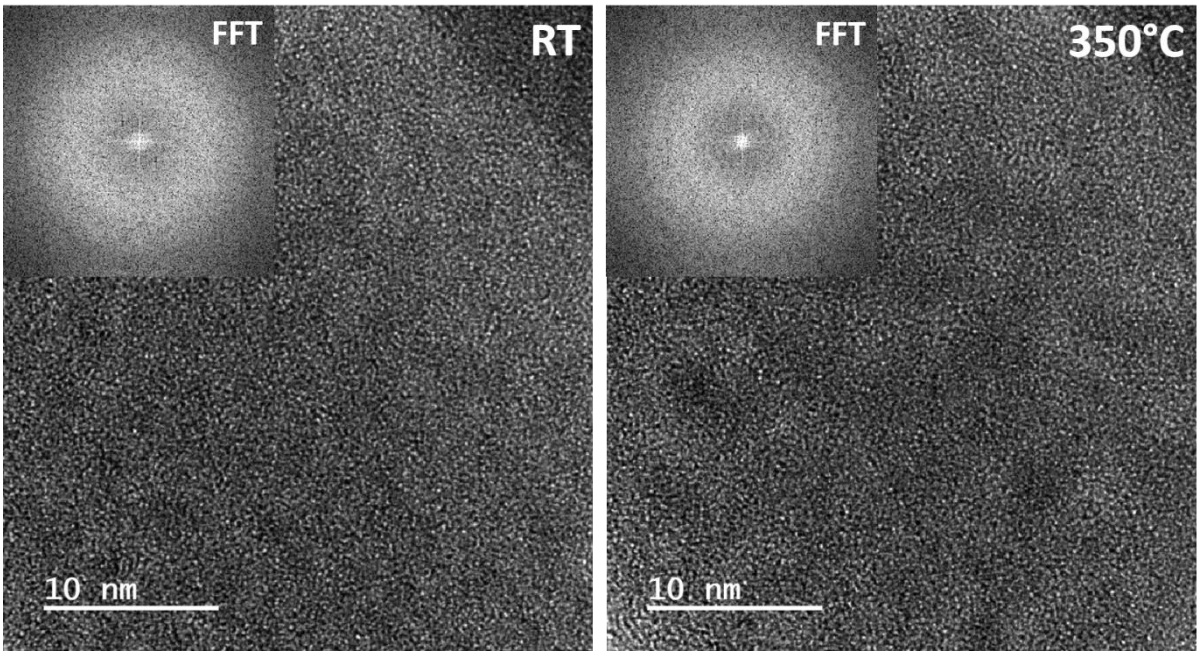

Figure 4. TEM micrographs acquired at room temperature and at 350 °C (intermediate temperatures are provided in Fig. S4) during variable-temperature in-situ TEM experiments performed on a T50 nanobead, manifesting a fully amorphous state (see the insets reporting the FFT of each image) and the concurrent intensification of contrast fluctuations.

To obtain a nanostructural view on the processes so far examined indirectly, the samples were characterized by in-situ TEM during thermal annealing (time-temperature traces are reported in Fig. S3). Microstructural changes mostly occurred during the heating ramps and not during isothermal plateaus, confirming the more crucial effect of temperature (rather than time) in activating crystallization processes[28]. Due to the major sample drift and focus shift exhibited by the samples (see also the videos provided as Supplementary Materials on zenodo.org, under the DOI: 10.5281/zenodo.7708900), it was however impossible to analyse images acquired during the heating ramps, which led us to concentrate on those collected during the far more stable isothermal dwells. Note that the first signs of crystal nucleation and long-range ordering were invariably identified by in-situ TEM at lower temperatures (at least by 200 or 300 °C) than by VT-XRD and VT-Raman, which can be partially attributed to the

superior detection capabilities of this technique but, most prominently, to the unavoidable energetic contribution of electron irradiation[20–22] to the processes. Apart from this observation, electron beam damage could be effectively avoided in the studied temperature range through a careful monitoring of the beam current density on the samples (see also Section 2.4).

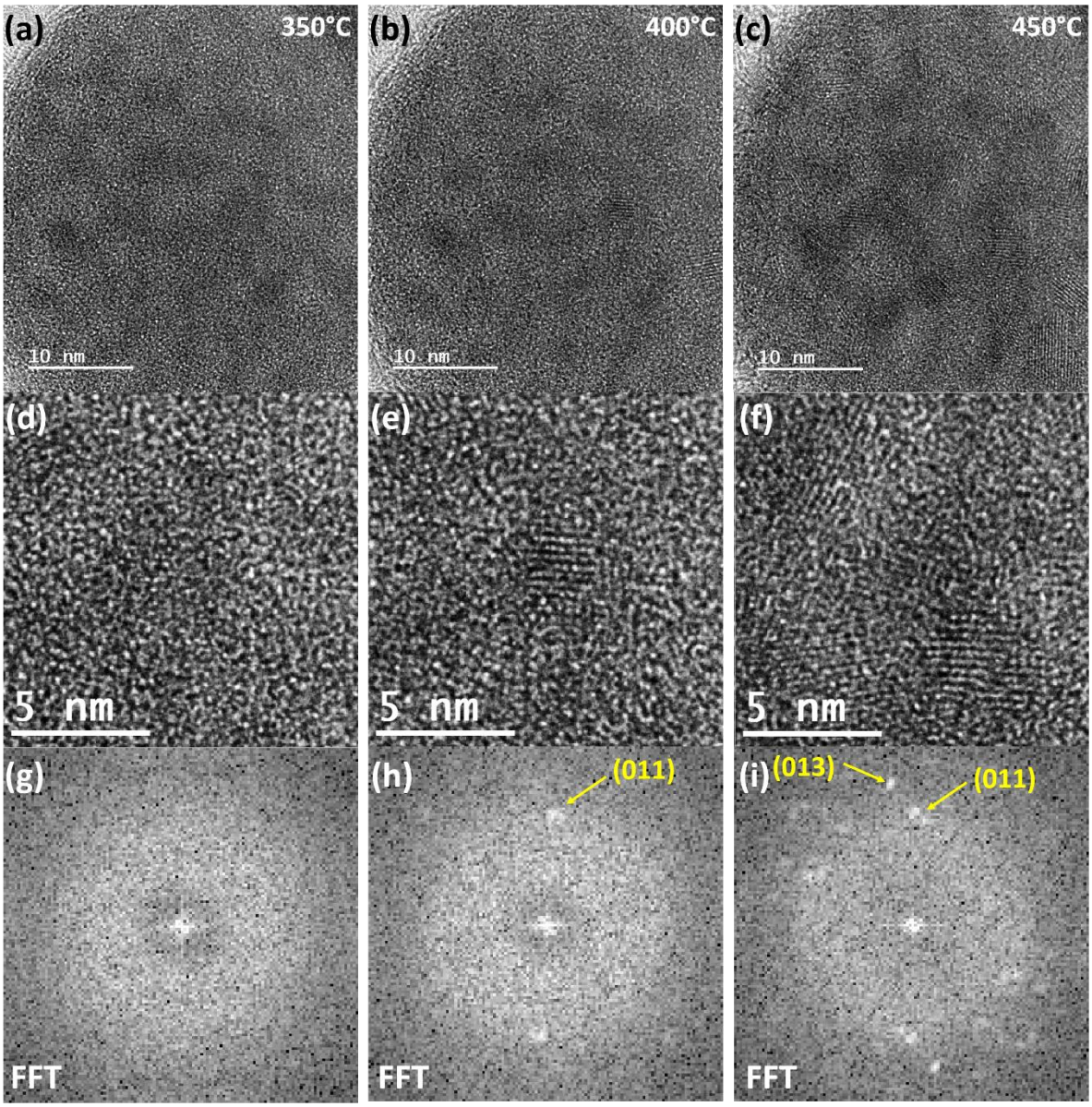

Figure 5. TEM micrographs acquired during in-situ TEM experiments at high temperature on a T50 nanobead at: a) 350 °C, b) 400 °C and c) 450 °C. A selected area of the same micrographs is presented at higher magnification (panels d,e,f) to document the emergence of nanocrystals within darker regions; these crystals are identified as anatase on the respective FFTs (panels g,h,i) reporting the assignment of the most intense diffraction spots to specific lattice planes. TEM micrographs acquired at temperatures up to 600 °C are provided on Figure S5 in the Supporting Information file.

Already before heating, the analysed amorphous T50 nanobead exhibit evident contrast modulations in the form of brighter and darker areas (Fig. 4 and S4), which were caused from

compositional fluctuations (i.e. heterogeneity) at the nanoscale (see also STEM results below). These high- and low-contrast regions grew to a diameter of several nanometers at 350 °C, until the darker ones gave rise at 400 °C to the formation of the first crystals (Fig. 5), whose size (3-5 nm) is in good agreement with the results obtained from VT-XRD at the beginning of crystallization (650 °C, see Fig. 2). Diffraction spots on fast Fourier-transformed (FFT) images were unambiguously assigned to the anatase structure [PDF 98-000-9852], also based on the above-presented complementary measurements. Their number gradually increased with temperature, indicating a more and more established crystalline state. Crystalline domains kept on growing, eventually achieving an average diameter of approximately 10 nm at 600 °C (Fig. S5), which is in good agreement with the results of VT-XRD, revealing a size of ~10 nm up to 800 °C and only later a marked growth up to 100 nm. The gradual growth of crystalline domains can be appreciated also from the videos provided as Supporting Materials on zenodo.org (DOI: 10.5281/zenodo.7708900), including FFTs of a large area of the sample. Nevertheless, the TEM heating experiment had to be arrested at 600 °C, as the examined nanobead appeared to eventually melt or evaporate under the electron beam. Back at room temperature after the experiment, the sample was checked at low magnification, revealing that even the carbon film supporting the nanobeads had been clearly damaged by the prolonged electron illumination in the measured area (Fig S6). Outside this region, the partially crystallized nanobeads still maintained their initial spherical shape, without evident signs of melting, confirming the limit (determined through preliminary tests) of ~600 °C for performing experiments in the absence of significant beam damage.

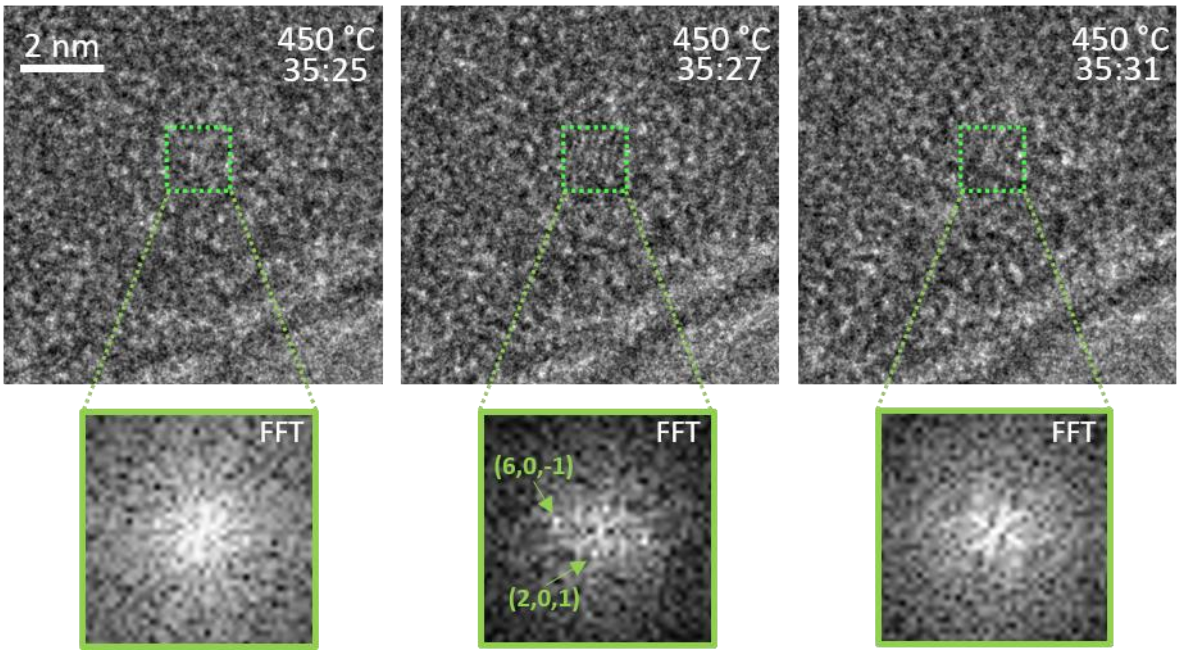

Figure 6. Magnification of TEM micrographs acquired at 450°C during a variable-temperature in-situ TEM experiment on a T17 nanobead (the full experiment is detailed in Fig. S7). They document the transient appearance of a crystalline nucleus with a size of ~1 nm over a few seconds (each micrograph reports the time elapsed from the start of the heating experiment). The respective FFTs report the assignment of the most intense diffraction spots to specific lattice planes in the TiO_2(B) structure.

The in-situ TEM experiment performed on sample T17 during heating yielded similar observations to those presented above: after an evident increase in size of high- and low-contrast regions (Figs. S7), crystals could be clearly identified at 600 °C, temperature at which the experiment was interrupted to avoid electron beam damage. The diffraction spots on FFT images acquired at 600 °C (Fig. S8) may equally be assigned to anatase or TiO_2(B) due to the strong structural similarities between these two phases[29], which were shown by VT-XRD to coexist in the sample up 1100 °C. The comparatively lower crystal volume density of T17 enabled moreover a more careful exploration of early crystallization stages during the post-processing, as exemplified in Figure 6: starting from 450 °C, we repeatedly observed the ephemeral appearance of crystalline nuclei with a minimum size of ~1 nm. They clearly generated defined spots on FFT images (*d*-spacings: 3.9(2) and 2.0(2) Å, assignable to the TiO_2(B) structure) but seemed to disappear after only a few seconds. The size of these crystalline nuclei corresponds to only few unit cell periodicities, since the lattice constants of monoclinic TiO_2(B) vary between 3.7412(2) Å along the *b* direction and 12.179(1) Å along the *a* direction[30].

It is tempting to associate these short-lived nanocrystals to the expected behaviour of subcritical crystalline nuclei[28], stochastically undergoing transient structural ordering/precipitation and dissolution/disordering before achieving full stabilization at a critical size. Theoretically, subcritical clusters can only transit to the critical region by randomly diffusing through their size space, as the driving force typically falls below the magnitude of kT (see definition of the Zeldovich factor in classical nucleation theory[31]). Assuming that the transition probability is the same in each direction, the width Δ of the critical size interval can therefore be approximated by the mean displacement of a colloidal particle in real space $\Delta^2 = 2Dt$, where D is the effective diffusion coefficient for this type of motion and $2t$ is the time needed for migration along the size axis through the critical interval[32]. Using $\Delta \approx 1$ nm and $t \approx 3$ s from Fig. 6, we obtain $D = 1.7 \times 10^{-19}$ m^2 s^{-1}, which agrees relatively well with the Ti and O diffusivities recently measured just above the glass transition in an aluminosilicate glass network[33]. In such a case, our work would represent the first direct TEM observation of subcritical nuclei, whose existence was previously only statistically inferred by fluctuation TEM[34,35]. Nonetheless, we cannot exclude that the short-lived appearance of these crystals may alternatively arise from slight focus changes during the dynamic heating experiment, also considering that the crystallites are surrounded by a residual amorphous phase.

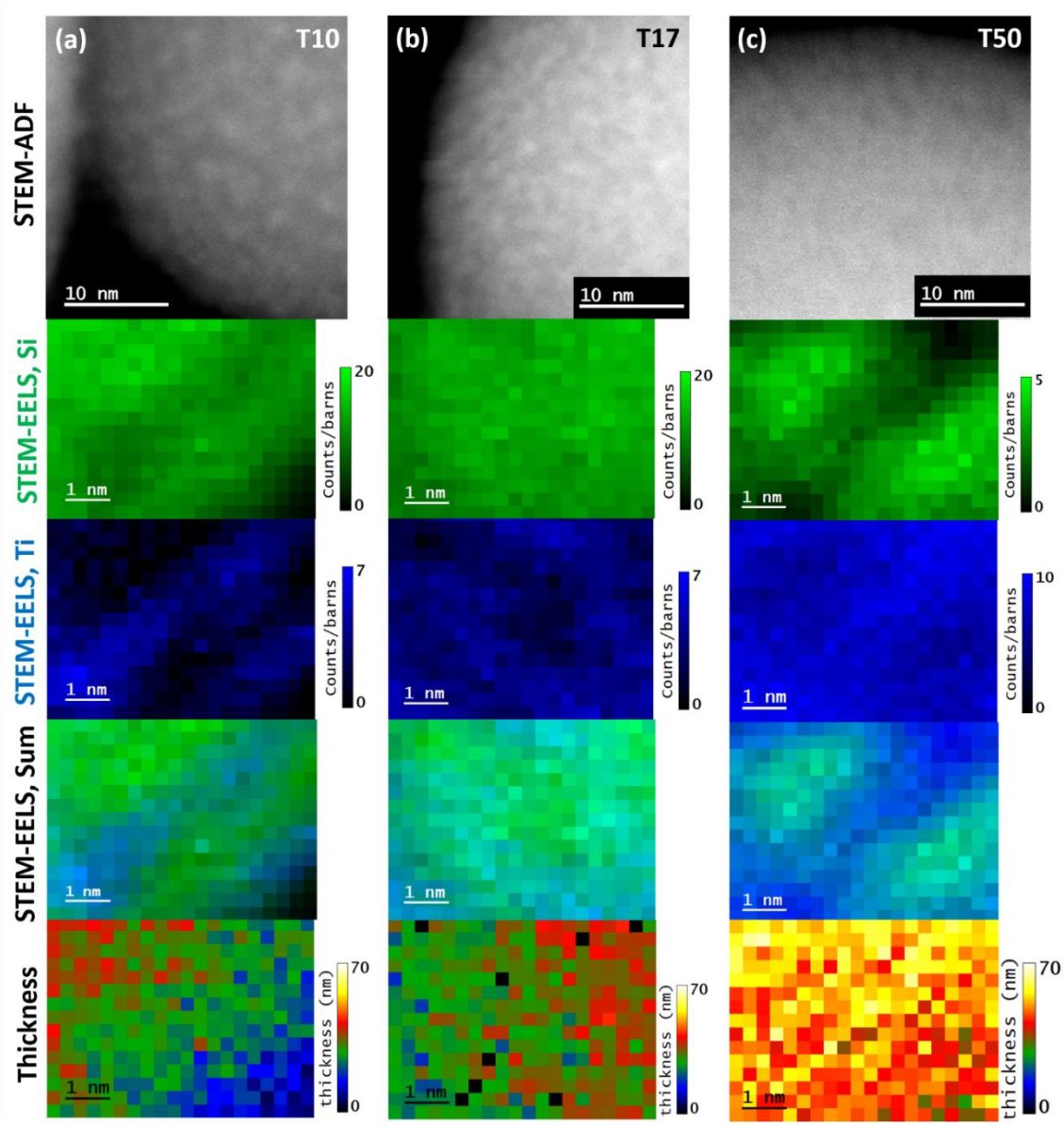

Figure 7. Micrographs acquired in STEM-ADF mode and STEM-EELS elemental mappings from thinner regions near the particle borders, manifesting the presence of nanoscale compositional heterogeneities in the as-prepared nanobeads: (a) T10, (b) T17 and (c) T50. Note the different scale between STEM-ADF images and elemental EELS maps. The estimated thickness of the analysed areas is also reported as color map.

In order to correlate the observed crystallization processes with the initial nanostructure of the glasses, we studied the as-sprayed samples also in STEM-ADF mode, in which image contrast is enhanced by differences in the local average chemical composition (Z-contrast). We combined these observations with spectrum imaging EELS (SI-EELS) analyses, to selectively map the areal distribution of Si and Ti in the nanobeads. In addition to samples T17 and T50, we synthesized and characterized also T10 (10 mol% TiO_2) to check whether a lower TiO_2 content would result in a significantly different degree of homogeneity at the nanoscale. All as-sprayed amorphous materials (Fig. 7) exhibited nanoscale contrast fluctuations with dark and bright areas (analogously to those observed during in-situ

TEM experiments in Fig. 4), respectively corresponding to regions enriched in elements with a lower or higher average atomic number. SI-EELS maps confirmed that these contrast modulations respectively originated from local enrichments in Si (Si_K: 105 eV) or Ti (Ti_L: 454 eV): their average composition (Tab. 1) exhibits a general increase in the amount of Ti in both the SiO_2- and the TiO_2-enriched regions going from T10 to T50, as expected from the nominal composition of the samples.

Table 1. Average compositions (at%) of chemical fluctuations identified in the as-sprayed nanobeads by SI-EELS. Also due to the thickness of the analysed samples, the uncertainty of the values is estimated at least as ± 5 at%.

Sample	SiO_2-enriched region		TiO_2-enriched region	
	Si (at%)	Ti (at%)	Si (at%)	Ti (at%)
T10 (as-sprayed)	100	0	67	33
T17 (as-sprayed)	90	10	68	32
T50 (as-sprayed)	38	62	7	93

Similar compositional fluctuations have been previously observed in melt-quenched ZrO_2-bearing glasses[17] and interpreted as the expression of an intrinsic tendency of these materials towards nanoscale heterogeneity, which could then play a major role during crystal nucleation. Transition metal oxides exhibit indeed limited solubility in undercooled melts[36–38] and their immiscibility-driven clustering is expected to start even during very fast quenching of the (assumedly homogeneous) stable superliquidus melt, at least until atomic mobility is kinetically hampered and frozen in (typically below the glass transition temperature). The samples analysed within this work were however synthesized by sol-gel spray-drying, which does not imply heating to very high temperature and could therefore potentially enable full homogenization down to the atomic scale. Nevertheless, problems with the homogenization of precursor solutions for the sol-gel synthesis of TiO_2-rich glasses are well-known in literature (see for instance[39,40]), so that similar phenomena cannot be excluded in this work despite having performed the synthesis according to a well-refined long-standing procedure[14]. All in all, both an incomplete mixing in solution or a possible incipient demixing during spray-drying at 200 °C would equally testify the strong driving force towards phase separation in SiO_2-TiO_2 materials, which can be kinetically hampered by the condensation into an interconnected glass but will inevitably proceed upon further thermal annealing. Note that compositional fluctuations are likely to be only slight in the as-sprayed state at least for T10, since Ti-O-Ti linkages (i.e. TiO_2 clustering) were below the limit of detection up to 8-10 mol% TiO_2 in similar samples recently investigated by Raman spectroscopy and solid-state magic-angle-spinning nuclear magnetic resonance (NMR) spectroscopy[16]. Samples T17 and T50 locate instead in a region of the SiO_2-TiO_2 phase diagram involving immiscibility even at very high temperature in the molten state[41], so that a certain degree of phase separation is not unexpected. Previous band gap measurements performed on photocatalytically active T17 nanobeads yielded values that were,

even in the amorphous state, close to but slightly higher than those of pure TiO_2 polymorphs[14], supporting the existence of TiO_2-enriched regions already in the as-sprayed materials.

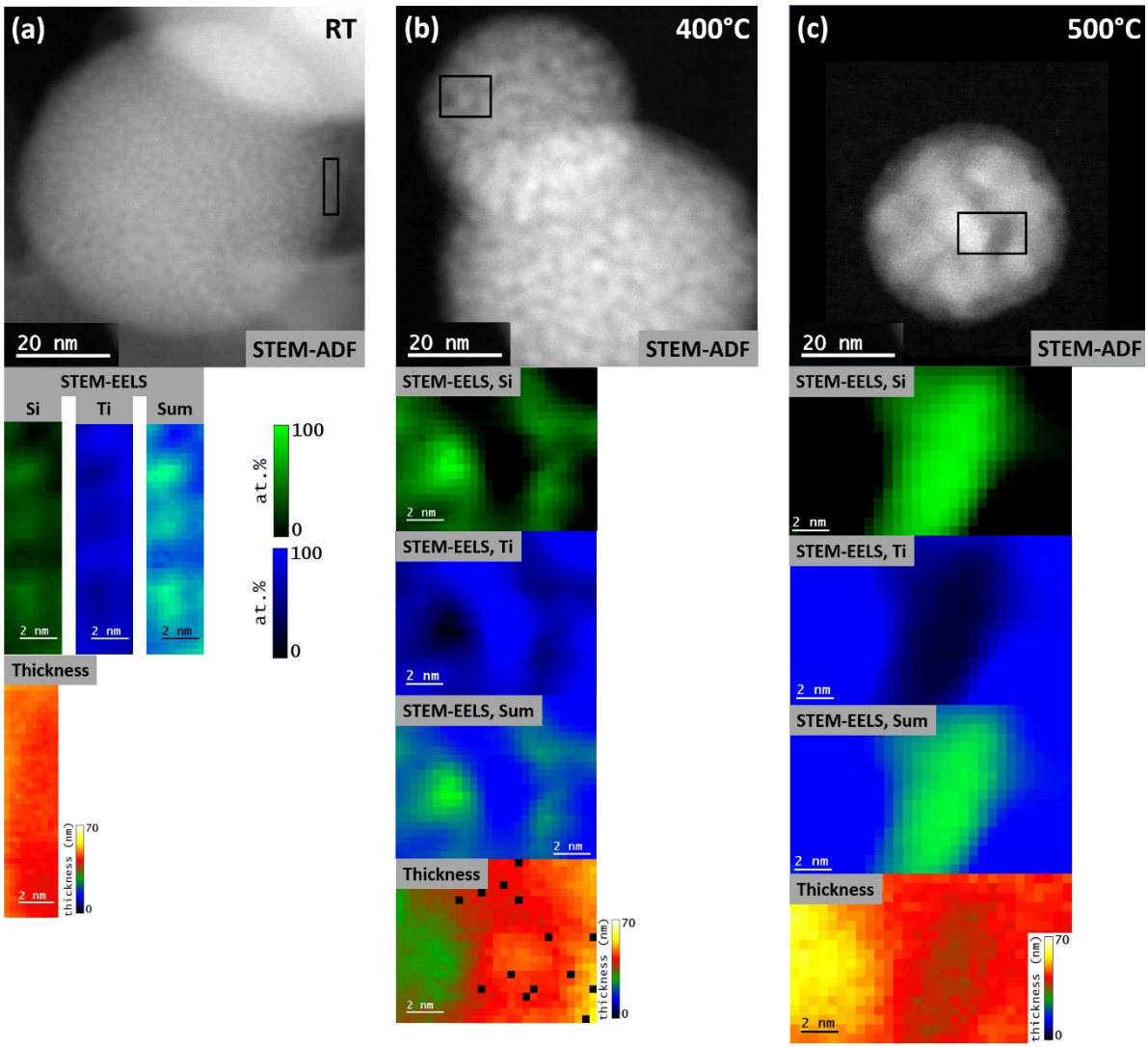

Figure 8. Micrographs acquired in STEM-ADF mode and STEM-EELS elemental mappings (from thinner regions near the particle borders), manifesting the growth of nanoscale compositional heterogeneities at various stages of heat treatment: (a) untreated, (b) treated to 400 °C and (c) treated to 500 °C. Note the different scale between STEM-ADF images and elemental EELS maps. The estimated thickness of the analysed areas is also reported as color map.

The evolution of the observed chemical fluctuations during thermal annealing of the starting nanobeads was examined through the acquisition of additional STEM-HAADF and SI-EELS data from sample T50, performing various subsequent heat treatments in situ in the TEM (Fig. 8). We observed a gradual growth in the amplitude and size of the compositional modulations with increasing temperature, reaching a maximum of 5–10 nm at 500 °C. As for their composition, it tended towards pure SiO_2 on the one hand and TiO_2 on the other hand already at 400 °C, in good agreement with the crystallization process detailed in TEM mode. It was therefore possible to experimentally confirm that long-range

chemical diffusion must be accomplished before the onset of long-range ordering, at least in this system involving non-isochemical crystal nucleation.

4. Conclusion

The combination of in-situ high-temperature analytical methods exhibiting complementary resolution (XRD, Raman spectroscopy and TEM) has yielded an unprecedentedly complete picture of crystallization processes driven by transition metal immiscibility in SiO_2-TiO_2 glasses during heat treatments. Summarizing the most relevant findings:

- Primary compositional fluctuations, already existing in the as-prepared glasses, were shown to play a major role in initiating and directing crystal nucleation.
- Such primary chemical modulations increased in size and amplitude before the first emergence of long-range order, signalling the key role of diffusion for non-isochemical crystallization processes.
- The ephemeral appearance of nanocrystals (diameter: 1 nm) at early stages of crystallization was interpreted as the possible first direct experimental observation of subcritical nuclei.
- Ostwald's rule of stages was confirmed to govern crystallization processes in glasses and the role of TiO_2(B) as a crucial "missing link" between amorphous and crystalline states in TiO_2-bearing glasses was reaffirmed.
- If experimental conditions are suitably evaluated to minimize beam damage, variable-temperature in-situ high-resolution TEM demonstrates an undeniable potential for the elucidation of crystallization processes in oxide glasses and glass-ceramics, opening up new perspectives for the study of transient nucleation stages.

Supporting information

In an .doc-file: details on the analysis of VT-XRD measurements (examples of Rietveld refinements); a DOI to retrieve from zenodo.org supplementary videos detailing the in-situ high-temperature TEM experiments; figures providing the time-temperature protocol followed during in-situ high-temperature TEM experiments; additional TEM micrographs of samples T17 and T50, acquired in-situ and at room temperature.

Acknowledgement

Alessio Zandonà wishes to acknowledge the Deutsche Forschungsgemeinschaft (DFG) for funding his research through the Walter Benjamin Program, project n. 448961237, ZA 1188/1-1 and ZA 1188/2-1. The authors are grateful to the ICMN laboratory (Orléans, France) for TEM access and to the French Agency for Research for its financial support through the Equipex Planex ANR-11-EQPX-36.

References

(1) Hartel, R. W. Advances in Food Crystallization. *Annu. Rev. Food Sci. Technol.* **2013**, *4* (1), 277–292. https://doi.org/10.1146/annurev-food-030212-182530.

(2) Chen, J.; Sarma, B.; Evans, J. M. B.; Myerson, A. S. Pharmaceutical Crystallization. *Crystal Growth & Design* **2011**, *11* (4), 887–895. https://doi.org/10.1021/cg101556s.

(3) Microstructure and Properties of Functional Ceramics. In *Microstructure, Property and Processing of Functional Ceramics*; Yin, Q., Zhu, B., Zeng, H., Eds.; Springer Berlin Heidelberg: Berlin, Heidelberg, 2010; pp 1–111. https://doi.org/10.1007/978-3-642-01694-3_1.

(4) Deubener, J.; Allix, M.; Davis, M. J.; Duran, A.; Höche, T.; Honma, T.; Komatsu, T.; Krüger, S.; Mitra, I.; Müller, R.; Nakane, S.; Pascual, M. J.; Schmelzer, J. W. P.; Zanotto, E. D.; Zhou, S. Updated Definition of Glass-Ceramics. *Journal of Non-Crystalline Solids* **2018**, *501*, 3–10. https://doi.org/10.1016/j.jnoncrysol.2018.01.033.

(5) Ivanov, Yu. P.; Meylan, C. M.; Panagiotopoulos, N. T.; Georgarakis, K.; Greer, A. L. In-Situ TEM Study of the Crystallization Sequence in a Gold-Based Metallic Glass. *Acta Materialia* **2020**, *196*, 52–60. https://doi.org/10.1016/j.actamat.2020.06.021.

(6) Lan, S.; Wei, X.; Zhou, J.; Lu, Z.; Wu, X.; Feygenson, M.; Neuefeind, J.; Wang, X.-L. In-Situ Study of Crystallization Kinetics in Ternary Bulk Metallic Glass Alloys with Different Glass Forming Abilities. *Appl. Phys. Lett.* **2014**, *105* (20), 201906. https://doi.org/10.1063/1.4901905.

(7) Sohn, S.; Jung, Y.; Xie, Y.; Osuji, C.; Schroers, J.; Cha, J. J. Nanoscale Size Effects in Crystallization of Metallic Glass Nanorods. *Nature Communications* **2015**, *6* (1), 8157. https://doi.org/10.1038/ncomms9157.

(8) Wang, L.; Chen, J.; Cox, S. J.; Liu, L.; Sosso, G. C.; Li, N.; Gao, P.; Michaelides, A.; Wang, E.; Bai, X. Microscopic Kinetics Pathway of Salt Crystallization in Graphene Nanocapillaries. *Phys. Rev. Lett.* **2021**, *126* (13), 136001. https://doi.org/10.1103/PhysRevLett.126.136001.

(9) Wang, T.; Lu, W.; Xu, X.; Qiu, J.; Yu, S. F. Study of Crystallization and Coalescence of Nanocrystals in Amorphous Glass at High Temperature. *Inorg. Chem.* **2019**, *58* (14), 9500–9504. https://doi.org/10.1021/acs.inorgchem.9b01491.

(10) Chung, S.-Y.; Kim, Y.-M.; Kim, J.-G.; Kim, Y.-J. Multiphase Transformation and Ostwald's Rule of Stages during Crystallization of a Metal Phosphate. *Nature Physics* **2009**, *5* (1), 68–73. https://doi.org/10.1038/nphys1148.

(11) Chung, S.-Y.; Kim, Y.-M.; Lee, S.; Oh, S. H.; Kim, J.-G.; Choi, S.-Y.; Kim, Y.-J.; Kang, S.-J. L. Cation Disordering by Rapid Crystal Growth in Olivine-Phosphate Nanocrystals. *Nano Lett.* **2012**, *12* (6), 3068–3073. https://doi.org/10.1021/nl300909h.

(12) Schultz, P. C. Binary Titania-Silica Glasses Containing 10 to 20 Wt% TiO2. *Journal of the American Ceramic Society* **1976**, *59* (5-6), 214–219. https://doi.org/10.1111/j.1151-2916.1976.tb10936.x.

(13) Baiker, A.; Dollenmeier, P.; Glinski, M.; Reller, A. Selective Catalytic Reduction of Nitric Oxide with Ammonia: II. Monolayers of Vanadia Immobilized on Titania—Silica Mixed Gels. *Applied Catalysis* **1987**, *35* (2), 365–380. https://doi.org/10.1016/S0166-9834(00)82873-0.

(14) Zandona, A.; Martínez Arias, A.; Gutbrod, M.; Helsch, G.; Weber, A. P.; Deubener, J. Spray-Dried TiO2(B)-Containing Photocatalytic Glass-Ceramic Nanobeads. *Advanced Functional Materials* **2021**, *31* (8), 2007760. https://doi.org/10.1002/adfm.202007760.

(15) Evans, D. L. Glass Structure: The Bridge between the Molten and Crystalline States. *Journal of Non-Crystalline Solids* **1982**, *52* (1–3), 115–128. https://doi.org/10.1016/0022-3093(82)90285-X.

(16) Zandonà, A.; Chesneau, E.; Helsch, G.; Canizarès, A.; Deubener, J.; Montouillout, V.; Fayon, F.; Allix, M. Glass-Forming Ability and Structural Features of Melt-Quenched and Gel-Derived SiO2-TiO2 Glasses. *Journal of Non-Crystalline Solids* **2022**, *598*, 121967. https://doi.org/10.1016/j.jnoncrysol.2022.121967.

(17) Dargaud, O.; Cormier, L.; Menguy, N.; Patriarche, G.; Calas, G. Mesoscopic Scale Description of Nucleation Processes in Glasses. *Appl. Phys. Lett.* **2011**, *99* (2), 021904. https://doi.org/10.1063/1.3610557.

(18) Coelho, A. A. TOPAS and TOPAS-Academic: An Optimization Program Integrating Computer Algebra and Crystallographic Objects Written in C++. *Journal of Applied Crystallography* **2018**, *51* (1), 210–218. https://doi.org/10.1107/S1600576718000183.
(19) Cheary, R. W.; Coelho, A. A Fundamental Parameters Approach to X-Ray Line-Profile Fitting. *Journal of Applied Crystallography* **1992**, *25* (2), 109–121. https://doi.org/10.1107/S0021889891010804.
(20) Albrecht, W.; van de Glind, A.; Yoshida, H.; Isozaki, Y.; Imhof, A.; van Blaaderen, A.; de Jongh, P. E.; de Jong, K. P.; Zečević, J.; Takeda, S. Impact of the Electron Beam on the Thermal Stability of Gold Nanorods Studied by Environmental Transmission Electron Microscopy. *Ultramicroscopy* **2018**, *193*, 97–103. https://doi.org/10.1016/j.ultramic.2018.05.006.
(21) Jiang, N. Beam Damage by the Induced Electric Field in Transmission Electron Microscopy. *Micron* **2016**, *83*, 79–92. https://doi.org/10.1016/j.micron.2016.02.007.
(22) Jiang, N. Electron Beam Damage in Oxides: A Review. *Reports on Progress in Physics* **2015**, *79* (1), 016501. https://doi.org/10.1088/0034-4885/79/1/016501.
(23) Zandona, A.; Patzig, C.; Rüdinger, B.; Hochrein, O.; Deubener, J. TiO2(B) Nanocrystals in Ti-Doped Lithium Aluminosilicate Glasses. *Journal of Non-Crystalline Solids: X* **2019**, *2*, 100025. https://doi.org/10.1016/j.nocx.2019.100025.
(24) Zhang, H.; F. Banfield, J. Thermodynamic Analysis of Phase Stability of Nanocrystalline Titania. *J. Mater. Chem.* **1998**, *8* (9), 2073–2076. https://doi.org/10.1039/A802619J.
(25) Ghosh, T. B.; Dhabal, S.; Datta, A. K. On Crystallite Size Dependence of Phase Stability of Nanocrystalline TiO2. *Journal of Applied Physics* **2003**, *94* (7), 4577–4582. https://doi.org/10.1063/1.1604966.
(26) Ostwald, W. Studien Über Die Bildung Und Umwandlung Fester Körper: 1. Abhandlung: Übersättigung Und Überkaltung. *Zeitschrift für Physikalische Chemie* **1897**, *22U* (1), 289–330. https://doi.org/doi:10.1515/zpch-1897-2233.
(27) Beuvier, T.; Richard-Plouet, M.; Brohan, L. Accurate Methods for Quantifying the Relative Ratio of Anatase and TiO $_2$ (B) Nanoparticles. *J. Phys. Chem. C* **2009**, *113* (31), 13703–13706. https://doi.org/10.1021/jp903755p.
(28) CHRISTIAN, J. W. CHAPTER 10 - The Classical Theory of Nucleation. In *The Theory of Transformations in Metals and Alloys*; CHRISTIAN, J. W., Ed.; Pergamon: Oxford, 2002; pp 422–479. https://doi.org/10.1016/B978-008044019-4/50014-3.
(29) Marchand, R.; Brohan, L.; Tournoux, M. TiO2(B) a New Form of Titanium Dioxide and the Potassium Octatitanate K2Ti8O17. *Materials Research Bulletin* **1980**, *15* (8), 1129–1133. https://doi.org/10.1016/0025-5408(80)90076-8.
(30) Feist, T. P.; Davies, P. K. The Soft Chemical Synthesis of TiO2 (B) from Layered Titanates. *Journal of Solid State Chemistry* **1992**, *101* (2), 275–295. https://doi.org/10.1016/0022-4596(92)90184-W.
(31) Zeldovich, Y. B. On the Theory of New Phase Formation: Cavitation. *Acta Physicochem. USSR* **1943**, *18*, 1.
(32) Gutzow, I. S.; Schmelzer, J. W. P. Kinetics of Crystallization and Segregation: Nucleation in Glass-Forming Systems. In *The Vitreous State: Thermodynamics, Structure, Rheology, and Crystallization*; Gutzow, I. S., Schmelzer, J. W. P., Eds.; Springer Berlin Heidelberg: Berlin, Heidelberg, 2013; pp 219–288. https://doi.org/10.1007/978-3-642-34633-0_6.
(33) Fielitz, P.; Helsch, G.; Borchardt, G.; Deubener, J. Al-26 and O-18 Tracer Diffusion in a Sodium Aluminosilicate Glass Coated with a TiO2 Layer. *Journal of Non-Crystalline Solids* **2023**, *under revision*.
(34) Lee, B.-S.; Burr, G. W.; Shelby, R. M.; Raoux, S.; Rettner, C. T.; Bogle, S. N.; Darmawikarta, K.; Bishop, S. G.; Abelson, J. R. Observation of the Role of Subcritical Nuclei in Crystallization of a Glassy Solid. *Science* **2009**, *326* (5955), 980–984. https://doi.org/10.1126/science.1177483.
(35) Darmawikarta, K.; Raoux, S.; Tchoulfian, P.; Li, T.; Abelson, J. R.; Bishop, S. G. Evolution of Subcritical Nuclei in Nitrogen-Alloyed Ge2Sb2Te5. *Journal of Applied Physics* **2012**, *112* (12), 124907. https://doi.org/10.1063/1.4770385.

(36) Zandonà, A.; Moustrous, M.; Genevois, C.; Véron, E.; Canizarès, A.; Allix, M. Glass-Forming Ability and ZrO2 Saturation Limits in the Magnesium Aluminosilicate System. *Ceramics International* **2021**. https://doi.org/10.1016/j.ceramint.2021.12.051.
(37) Zandonà, A.; Ory, S.; Genevois, C.; Véron, E.; Canizarès, A.; Pitcher, M. J.; Allix, M. Glass Formation and Devitrification Behavior of Alkali (Li, Na) Aluminosilicate Melts Containing TiO2. *Journal of Non-Crystalline Solids* **2022**, *582*, 121448. https://doi.org/10.1016/j.jnoncrysol.2022.121448.
(38) Scarani, A.; Zandonà, A.; Di Fiore, F.; Valdivia, P.; Putra, R.; Miyajima, N.; Bornhöft, H.; Vona, A.; Deubener, J.; Romano, C.; Di Genova, D. A Chemical Threshold Controls Nanocrystallization and Degassing Behaviour in Basalt Magmas. *Communications Earth & Environment* **2022**, *3* (1), 284. https://doi.org/10.1038/s43247-022-00615-2.
(39) Schraml-Marth, M.; Walther, K. L.; Wokaun, A.; Handy, B. E.; Baiker, A. Porous Silica Gels and TiO2/SiO2 Mixed Oxides Prepared via the Sol-Gel Process: Characterization by Spectroscopic Techniques. *Journal of Non-Crystalline Solids* **1992**, *143*, 93–111. https://doi.org/10.1016/S0022-3093(05)80557-5.
(40) Delattre, L.; Babonneau, F. 17O Solution NMR Characterization of the Preparation of Sol−Gel Derived SiO2/TiO2 and SiO2/ZrO2 Glasses. *Chem. Mater.* **1997**, *9* (11), 2385–2394. https://doi.org/10.1021/cm970372f.
(41) DeVries, R. C.; Roy, R.; Osborn, E. F. Phase Equilibria in the System CaO-TiO2–SiO2. *Journal of The American Ceramic Society* **1955**, *38* (5), 158–171.